Capillarity

Vol. 11, No. 1, p. 22-30, 2024

Original article

Prediction of displacement patterns in porous media using the probability of pore-scale filling events

Tian Lan[1,2]*, Ran Hu[1,2]

[1]*State Key Laboratory of Water Resources Engineering and Management, Wuhan University, Wuhan 430072, P. R. China*

[2]*Key Laboratory of Rock Mechanics in Hydraulic Structural Engineering of the Ministry of Education, Wuhan University, Wuhan 430072, P. R. China*

Keywords:
Multiphase flow
displacement patterns
porosity
disorder
pore-filling events

Cited as:
Lan, T., Hu, R. Prediction of displacement patterns in porous media using the probability of pore-scale filling events. Capillarity, 2024, 11(1): 22-30.
https://doi.org/10.46690/capi.2024.04.02

Abstract:
Multiphase flow in porous media is a common process in numerous engineering applications. While numerous studies have been conducted to investigate the impact of flow conditions, fluid properties, and wettability, the influence of flow geometry on the flow process remains poorly understood. Here, a theoretical model is proposed to directly forecast the displacement patterns across a wide range of porosity and disorder. This model is built upon the revelation that the overlap event stabilizes the invasion front, allowing us to predict displacement patterns by computing the probability of the overlap event. A value of 1 indicates a stable invasion process, resulting in compact displacement. Conversely, a value of 0 signifies an unstable invasion process, leading to capillary fingering. In the intermediate range between 0 and 1, a crossover zone is observed. The predicted phase diagram is evaluated using pore-network simulations and experiments in the literature, confirming that this model can reasonably predict displacement patterns under varying porosity and disorder. This contribution extends classical phase diagrams and holds practical significance for engineering applications.

1. Introduction

Immiscible fluid displacement is a prevalent phenomenon in various engineering applications, including geological carbon sequestration (Ershadnia et al., 2020; Wang et al., 2023; Wei et al., 2023), enhanced oil recovery (Li et al., 2020; Morrow and Mason, 2001; Pi et al., 2023), groundwater contamination by non-aqueous liquids (Dawson and Roberts, 1997), and water removal in the cathode gas diffusion layer of PEM fuel cell (Tang et al., 2007). In the context of multiphase flow with a fluid-fluid interface, the stability of the front interface holds paramount importance, as it significantly impacts displacement patterns and efficiency (Paterson, 1981; Glass et al., 2001; Armstrong and Berg, 2013; Bischofberger et al., 2014; Cai et al., 2021; Zhao et al., 2023).

In the absence of gravity effects, the instability of the front interface is governed by viscous and capillary forces (Måløy et al., 1985; Babchin et al., 2008; Cottin et al., 2011; Molnar et al., 2020; Geistlinger and Zulfiqar, 2020). Lenormand et al. (1988) pioneered the development of a phase diagram to characterize fluid-fluid displacement in a porous medium using two dimensionless parameters: the viscous ratio ($M = \mu_i/\mu_d$) and the capillary number ($\mathrm{Ca} = \mu_i v/\gamma$). Here, μ_i and μ_d represent the dynamic viscosities of the invading and defending fluids, respectively, v is the characteristic velocity, and γ is the interfacial tension. For $M > 1$, displacement patterns transition from capillary fingering (CF) to compact displacement (CD) with increasing Ca. Conversely, for $M < 1$, displacement patterns shift from CF to the crossover zone (CZ) and eventually to viscous fingering (Chen et al., 2017). However, this phase diagram does not incorporate the impact of flow geometry and is applicable solely under drainage conditions.

*Corresponding author.
E-mail address: lantian@whu.edu.cn (T. Lan); whuran@whu.edu.cn (R. Hu).

Yandy Scientific Press

Received December 8, 2023; revised December 29, 2023; accepted January 18, 2024; available online January 22, 2024.

Under imbibition conditions, the fluid-fluid interface invasion becomes notably intricate (Cai et al., 2010, 2014; Hu et al., 2018; Singh et al., 2019). Menisci motion is influenced not only by Haines jumps (bursts) but also controlled by additional modes such as touches and overlaps (Cieplak and Robbins, 1988, 1990; Zhao et al., 2016, 2019; Primkulov et al., 2021). Specifically, the existence of overlap contributes to stabilizing the front interface (Holtzman and Segre, 2015; Hu et al., 2019; Lan et al., 2020). As the wetting phase contact angle (θ) decreases to around 45°, and at lower Ca, displacement patterns demonstrate CD rather than CF.

On the other hand, flow geometry also influences the instability of the front interface (Spaid and Phelan, 1998; Geiger-Boschung et al., 2009; de Anna et al., 2017; Svidrytski et al., 2018; Nijjer et al., 2019). Given the intricate nature and diverse characteristics of porous media, research in this domain remains inadequately comprehensive (Lewandowska et al., 2005; Borgman et al., 2017; Fantinel et al., 2017; Suo et al., 2020). Recent investigations have predominantly concentrated on disordered and ordered porous media. In the context of disordered porous media, prior research has indicated that reducing disorder stabilizes the invasion front for both drainage and imbibition processes (Chen and Wilkinson, 1985; King, 1987; Toussaint et al., 2005; Holtzman, 2016; Wu et al., 2021). A recent systematic study explored the combined impact of disorder and wettability on displacement patterns (Hu et al., 2019). The findings demonstrated that the influence of disorder varies with alterations in wettability. Under diverse wettability conditions, an increase in disorder can result in either the stabilization or destabilization of the invasion front.

Other studies have examined ordered porous media, characterized by variations in porosity along the flow direction, to comprehend their influence on displacement patterns (Al-Housseiny et al., 2012; Rabbani et al., 2018; Lu et al., 2019; Lan et al., 2022a, 2022b). Rabbani et al. (2018) observed that a linear variation in porosity corresponds to linear variations in viscous and capillary forces, manifesting specific flow patterns, such as single fingering. Lu et al. (2019) and Lan et al. (2022a) further investigated the interplay between porosity gradient and disorder, revealing that a sufficiently large gradient can completely mitigate the impact of disorder. Wang et al. (2022) explored the influence of porosity on multiphase flow in regular porous media, finding that decreasing porosity leads to a transition in displacement patterns from CD to CF. These studies underscore the significance of porosity, in addition to disorder, in multiphase flow. Nonetheless, additional research is necessary to elucidate the combined influence of porosity and disorder on displacement patterns.

In this study, pore-network simulations and theoretical analysis are combined to explore the influence of porosity and disorder on displacement patterns. Considering that overlap events stabilize the invasion front, a theoretical model is introduced to predict displacement patterns by evaluating the probability of overlap occurrences. The model produces phase diagrams illustrating displacement patterns under varied porosity and disorder conditions. Validation of theoretical predictions is accomplished through numerical simulations and referenced experiments. This study holds significant implications for advancing our comprehension of multiphase flow control in porous media.

2. Predictive method

2.1 Pore-filling events

The pore-filling events of bursts, touches, and overlaps were initially introduced by Cieplak and Robbins (1988, 1990) to depict the motion of the meniscus in porous media. The determination of the critical radius of curvature for these three pore-filling events has been addressed in our previous work (Hu et al., 2019). Here, a concise overview of the equations for the three pore-filling events is provided.

The burst event and touch event involve a single meniscus. The burst event occurs when the capillary pressure reaches its maximum value, beyond which no stable meniscus can exist (Fig. 1(a)). The critical radius of the burst event (R_b) can be expressed as:

$$R_b = \frac{-b_1 + \sqrt{b_1^2 - 4a_1c_1}}{2a_1} \tag{1}$$

where a_1, b_1, c_1 are the coefficients given in Table 1.

The touch event occurs when the meniscus comes into contact with the edge of the nearest post (Fig. 1(b)). The critical radius of the touch event (R_t) is formulated as:

$$R_t = \frac{-b_2 + \sqrt{b_2^2 - 4a_2c_2}}{2a_2} \tag{2}$$

where a_2, b_2, c_2 are the coefficients given in Table 1.

To determine the sequence of the burst event and touch event, a particular fluid reconfiguration is examined, wherein the meniscus attains its minimum radius of curvature upon touching the nearest post (Fig. 1(c)). The critical radius of curvature (R_c) is expressed as:

$$R_c = \frac{a^2 + r_1^2 + r_2^2 - 2r_3^2}{4r_3 + 2(r_1 + r_2)\cos\theta} \tag{3}$$

where r_1, r_2, and r_3 are the radii of posts 1, 2, and 3, respectively, and a is the distance between the centers of two adjacent posts. If $R_b < R_c$, the burst event precedes the touch event. Conversely, if $R_b > R_c$, the meniscus contacts the edge of the nearest post before the burst event occurs.

The overlap event entails multiple menisci. When neighboring menisci make contact at the three-phase contact point, they merge to form a new meniscus (Fig. 1(d)). The condition for the overlap event an be expressed as:

$$\angle O_1O_2O_4 \le 2\alpha - \beta_1 - \beta_2 \tag{4}$$

and the critical radius of curvature of the overlap event (R_o) can be calculated by:

$$\angle O_1O_2O_4 = 2\alpha - \beta_1 - \beta_2 \tag{5}$$

where the expressions for α, β_1, and β_2 are given in Table 1.

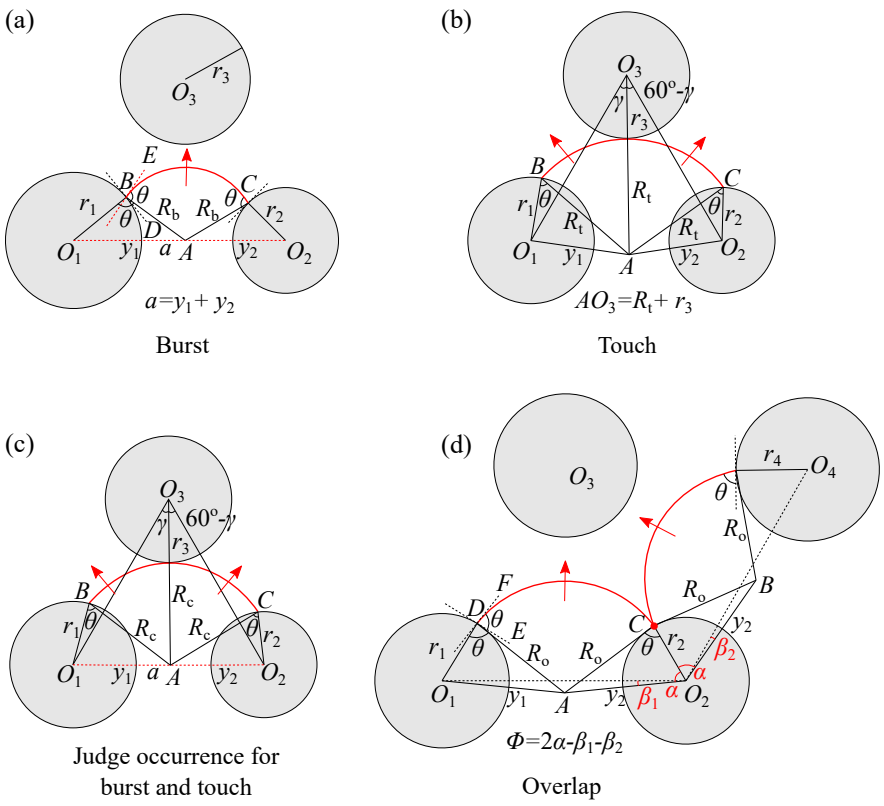

Fig. 1. Geometry for calculating the radii of curvature of menisci for three pore-filling events. (a) The burst event occurs when the radius of curvature reaches its minimum value (corresponding to the maximum capillary pressure), (b) the touch event occurs as the meniscus makes contact with the edge of the nearest post, (c) the critical condition for determining the occurrence of the burst event and touch event, and (d) the overlap event occurs when two neighboring menisci contact at the three-phase contact point. The red arcs depict the fluid-fluid interface, and the red arrows indicate the direction of menisci motion.

Table 1. Coefficients in Eqs. (1)-(5).

Modes	Coefficients
Burst	$a_1 = 2-\frac{2}{a^2}(r_1-r_2)^2\cos^2\theta$
	$b_1 = \frac{2}{a^2}(r_1-r_2)^2(r_1+r_2)\cos\theta - 2(r_1+r_2)\cos\theta$
	$c_1 = r_1^2+r_2^2-\frac{a^2}{2}-\frac{1}{2a^2}(r_1^2-r_2^2)^2$
Touch	$a_2 = 4r_3^2+4\cos^2\theta(r_1^2+r_2^2-4r_1r_2)+4r_3\cos\theta(r_2+r_1)-3a^2$
	$b_2 = 2a^2(r_1\cos\theta+r_2\cos\theta-2r_3)+2r_1\cos\theta(r_2^2+r_3^2-2r_1^2)+2r_2\cos\theta(r_1^2+r_3^2-2r_2^2)+2r_3(2r_3^2-r_1^2-r_2^2)$
	$c_2 = a^2(a^2-r_1^2-r_2^2-r_3^2)+\frac{1}{2}(r_1^2-r_2^2)^2+\frac{1}{2}(r_1^2-r_3^2)^2+\frac{1}{2}(r_2^2-r_3^2)^2$
Overlap	$\alpha = \cos^{-1}\left(\frac{r_2-R_o\cos\theta}{\sqrt{r_2^2+R_o^2-2r_2R_o\cos\theta}}\right)$
	$\beta_1 = \cos^{-1}\left[\frac{a^2+r_2^2-r_1^2+2(r_1-r_2)R_o\cos\theta}{2a\sqrt{r_2^2+R_o^2-2r_2R_o\cos\theta}}\right]$
	$\beta_2 = \cos^{-1}\left[\frac{a^2+r_2^2-r_4^2+2(r_4-r_2)R_o\cos\theta}{2a\sqrt{r_2^2+R_o^2-2r_2R_o\cos\theta}}\right]$

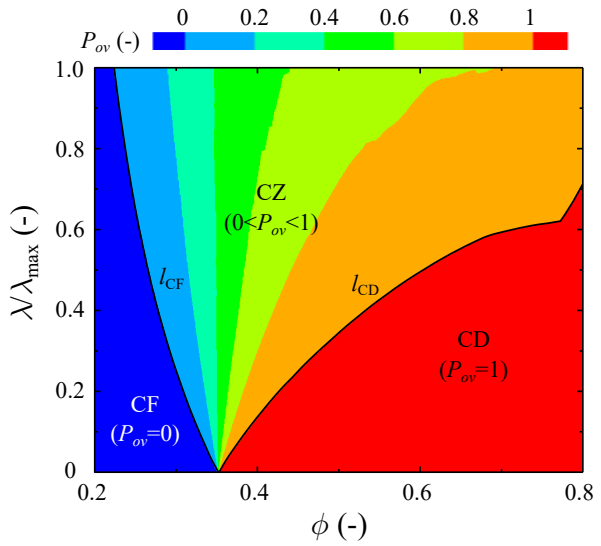

Fig. 2. Variation of overlap probability (P_{ov}) with porosity (ϕ) and normalized disorder index ($\lambda/\lambda_{\max}$). The overlap probability (P_{ov}) is visually represented in red for higher values and blue for lower values, serving to classify different displacement patterns. The displacement patterns include CD for $P_{ov}=1$, the CZ for $0<P_{ov}<1$, and CF for $P_{ov}=0$. The boundary curves l_{CD} and l_{CF} demarcate the transition from CD to CZ to CF.

2.2 Phase diagram under varying porosity and disorder

Section 2.1 describes the identification and critical radius of curvature calculation for pore-filling events in a four-post system (Fig. 1(d)). Given that the burst and touch events consistently yield an irregular invasion morphology, in contrast to the overlap event, which produces a compact invasion front (Holtzman and Segre, 2015; Singh et al., 2019), the displacement pattern can be anticipated by evaluating the probability of the overlap event, denoted as P_{ov} (Hu et al., 2019).

Initially, the probability density function is computed, denoted as $f(r)$, for a post radius. This study assumes a uniformly distributed geometry, with the posts' radius (r_i) defined as:

$$r_i \sim U[(1-\lambda)\bar{r},(1+\lambda)\bar{r}] \tag{6}$$

where λ is the disorder index, and $\bar{r}$ is the average radius of posts, which is related to porosity (ϕ) and can be calculated by:

$$\bar{r}=\sqrt{\frac{\sqrt{3}a^2(1-\phi)}{2\pi}} \tag{7}$$

The probability density function, $f(r)$, for the post radius distribution is expressed as:

$$f(r)=\begin{cases}\dfrac{1}{2\lambda\bar{r}}, & r\in[(1-\lambda)\bar{r},(1+\lambda)\bar{r}]\\ 0, & \text{else}\end{cases} \tag{8}$$

For a four-post system (r_1, r_2, r_3, and r_4), the probability density function for the system distribution is determined as follows:

$$f(r_1,r_2,r_3,r_4)=\begin{cases}(2\lambda\bar{r})^{-4}, & (r_1,r_2,r_3,r_4)\in G\\ 0, & \text{else}\end{cases} \tag{9}$$

where $G=\{(r_1,r_2,r_3,r_4):(1-\lambda)\bar{r}\le r_i\le(1+\lambda)\bar{r},\ i=1,2,3,4\}$ is a bounded closed region with a volume of $(2\lambda\bar{r})^4$. As the occurrence of the overlap event can be determined by Eq. (4), the probability of the overlap event for an arbitrary four-post system can be expressed as:

$$P_{ov}=\iiint\int_{G\cap G_{ov}}(2\lambda\bar{r})^{-4}\,\mathrm{d}r_1\,\mathrm{d}r_2\,\mathrm{d}r_3\,\mathrm{d}r_3 \tag{10}$$

where G_{ov} is the bounded closed region in which the overlap event occurs and is defined as:

$$G_{ov}(\lambda,\phi,\theta)=\{(r_1,r_2,r_3,r_4):2\alpha(\lambda,\phi,\theta)-\beta_1(\lambda,\phi,\theta)-\beta_2(\lambda,\phi,\theta)\ge\frac{2\pi}{3}\} \tag{11}$$

The theoretical model (Eq. (9)) can predict displacement patterns under different contact angles, disorder, and porosity. However, the specific influence of contact angles on displacement patterns is not within the focus of this study. Consequently, we have opted to showcase results for a singular contact angle ($\theta=60^\circ$) while considering fluctuations in porosity ($0.2\le\phi\le0.8$) and disorder ($0\le\lambda/\lambda_{\max}\le1$), as illustrated in Fig. 2. The transition of the displacement patterns from CF to the CZ to CD is delineated by the boundary curves l_{CF} and l_{CD}. The inflection point in l_{CD} arises due to the shift from a single pore-filling event dominated by the touch event to being dominated by the burst event. When the porosity is below the boundary curve l_{CF} (blue area in Fig. 2), $P_{ov}=0$, and only the burst and touch events occur. In this case, the invasion front is irregular, and the displacement pattern exhibits CF. When the porosity is above the boundary curve l_{CD} (red area in Fig. 2), $P_{ov}=1$, and the overlap event occurs in all four-post systems, resulting in a stable invasion front and CD. For porosities between the two curves, the competing effects lead to the CZ. Consequently, the displacement patterns at varying porosities and disorders are predicted.

3. Evaluation of the predicted model

3.1 Overview of the pore-network model

The predicted model is evaluated using a pore-network model previously introduced in studies by Hu et al. (2019) and Lan et al. (2020). This pore-network model has been experimentally validated in prior research. Originally proposed by Cieplak and Robbins (1988, 1990), the model has undergone enhancements in subsequent studies (Holtzman and Segre, 2015; Primkulov et al., 2018, 2019; Zhao et al., 2019; Lan et al., 2022a).

The pore-network system is comprised of posts, throats, and pores. As depicted in Fig. 3, the grey circles in the diagram represent posts arranged in a triangular lattice, maintaining a constant distance of $a=250$ μm. Each set of three adjacent posts forms a pore, and the dashed line between two pores

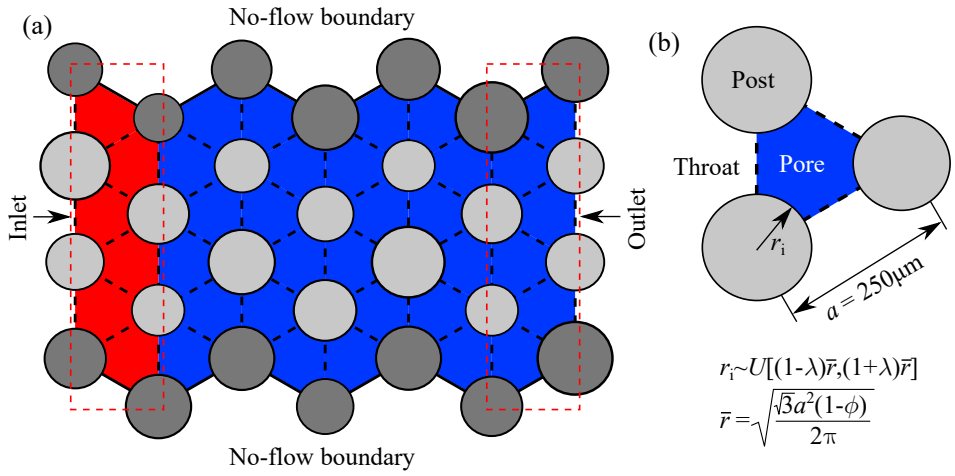

Fig. 3. Schematic diagram of pore-network model. (a) Initially, all pores are filled with the defending phase (blue), except for the pores at the inlet, which are filled with the invading phase (red). The upper and lower boundaries are designated as the no-flow boundary and (b) The grey circles represent posts arranged in a triangular lattice with a distance of $a = 250$ μm. The post radius follows a uniform distribution $r_i \sim U[(1-\lambda)\bar{r},(1+\lambda)\bar{r}]$ where $\bar{r} = \sqrt{\sqrt{3}a^2(1-\phi)/(2\pi)}$ is the average radius, and ϕ is the porosity of the porous medium. Three posts form a pore, and the dashed line between two pores represents the throat.

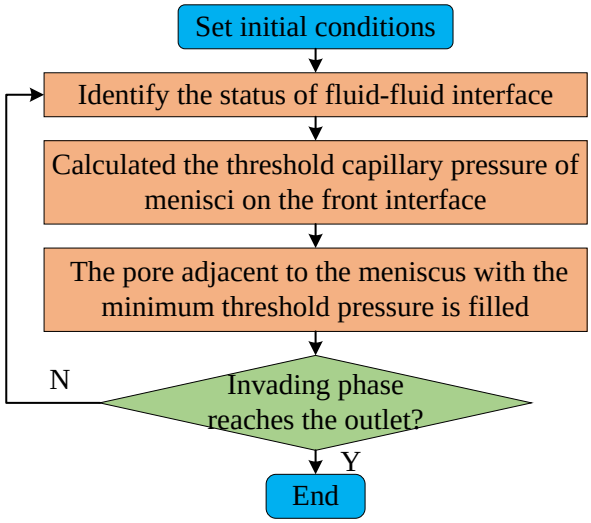

Fig. 4. Flow chart of pore-network model. The threshold capillary pressure is calculated using the pore-filling events depicted in Fig. 1. At each step, the pore with the lowest threshold capillary pressure is invaded. The simulation concludes when any pore in the outlet is filled.

represents the throat (Fig. 3(b)). The flow chart of the pore-network model is presented in Fig. 4. Initially, all pores are filled with the defending phase, while the invading phase occupies the pores at the inlet. The upper and lower boundaries are designated as no-flow boundaries. In each simulation cycle, the fluid-fluid interface's flowing state is initially determined. The interface is identified based on the pore-filling state and then separated into the front interface (flowable) and the trapped interface (non-flowable). Next, the threshold capillary pressure for all menisci on the front interface is calculated using Eqs. (1)-(5). The pore adjacent to the meniscus with the minimum threshold capillary pressure, initially filled by the defending phase, becomes filled by the invading phase. By repeating these steps until any pore in the outlet is filled by the invading phase, the quasi-static fluid invasion process in the porous media is simulated.

As the pore-network model is specifically devised for a two-dimensional (2D) system, the simulation does not account for the fluid advancements with three-dimensional characteristics, along with associated mechanisms such as corner flow (Dong and Chatzis, 1995; Weislogel and Lichter, 1998), snap-off (Roof, 1970), and spreading of thin wetting films (Levaché and Bartolo, 2014; Odier et al., 2017). These crucial mechanisms typically play a significant role in displacement processes under strong imbibition conditions ($\theta < 45°$) (Concus and Finn, 1969). Consequently, the applicability of this pore-network model is limited to 2D porous media with $\theta > 45°$.

3.2 Evaluation using numerical simulations

Pore-network simulations are conducted within the same parameter range as the predicted phase diagram of displacement patterns (Fig. 2), namely $\theta = 60°$, $0.2 \leq \phi \leq 0.8$, and $0 \leq \lambda/\lambda_{max} \leq 1$. $\phi \times \lambda/\lambda_{max} = 7 \times 6 = 42$ conditions are considered, with 10 independently generated geometries for each condition, totaling 420 computational cases.

For the purpose of comparison with the theoretical model, the typical displacement patterns under each condition are illustrated in Fig. 5, while the saturation (S_{br}) and the fractal dimension (D_f) of the simulation at the breakthrough time are depicted in Fig. 6. The predicted boundaries l_{CF} and l_{CD} indicating the transition from CF to the CZ and to CD are also presented in Fig. 6. Displacement patterns are characterized using invasion morphology, saturation (S_{br}), and D_f. In CF, the invasion front is unstable, resulting in minimum values

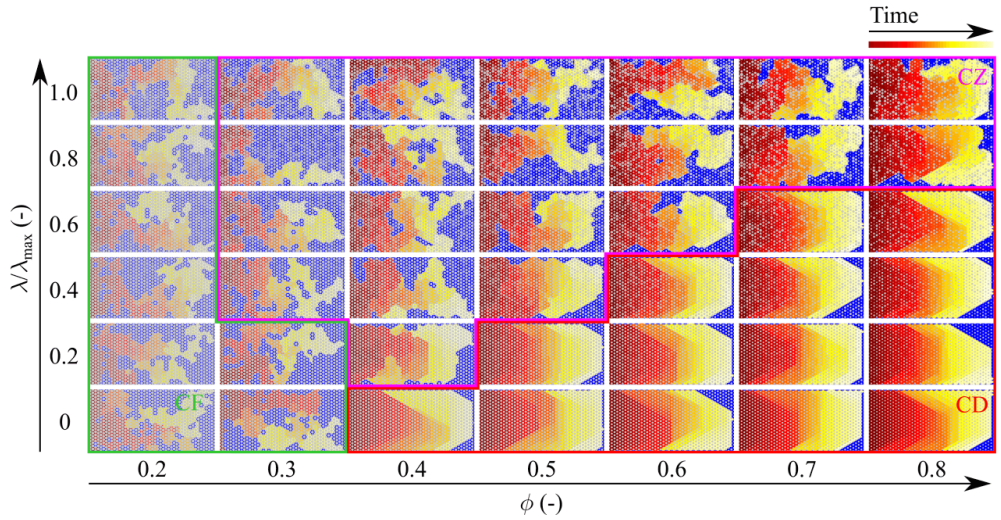

Fig. 5. Simulated displacement patterns at various porosities (ϕ) and normalized disorder indices (λ/λ_{max}), covering the range $0.2 \leq \phi \leq 0.8$ and $0 \leq \lambda/\lambda_{max} \leq 1$. The flow direction is from left to right. Colors ranging from dark red to yellow represent the initial stage to the breakthrough time. As porosity (ϕ) increases, the displacement patterns translate from CF to the CZ and ultimately to CD. The extent of the CZ expands with increasing disorder.

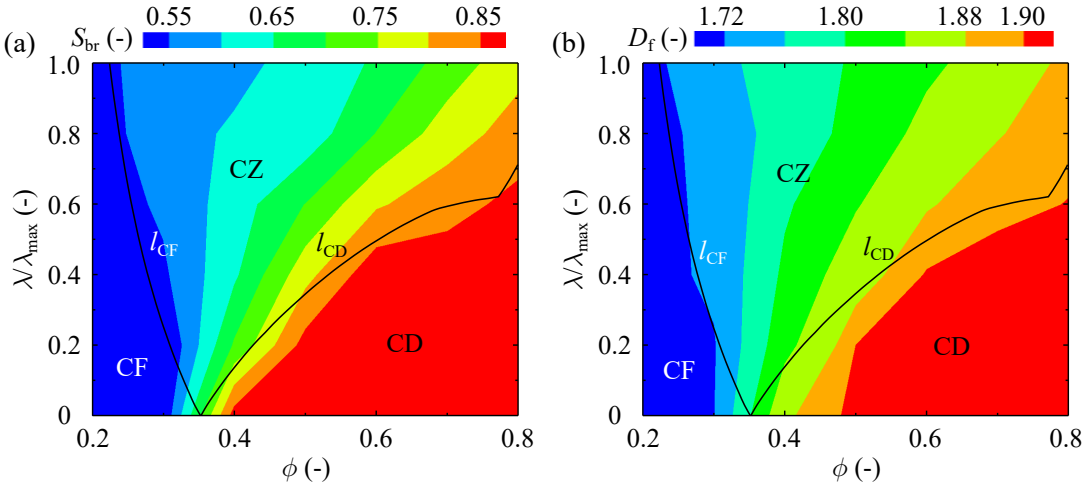

Fig. 6. Phase diagram of displacement patterns in the $\phi - \lambda/\lambda_{max}$ plane, where ϕ varying from 0.2 to 0.8 and λ/λ_{max} varying from 0 to 1. The evaluation of the phase diagram includes invading fluid saturation S_{br} (a) and fractal dimension D_f (b) at the time of breakthrough.

of S_{br} (≤ 0.55) and D_f (≤ 1.72) (Fig. 6). CD features a stable invasion front, reaching maximum S_{br} (≥ 0.85) and D_f (≥ 1.90) values (Fig. 6). The CZ witnesses the transition from an unstable to a stable invasion front, with $0.55 \leq S_{br} \leq 0.85$ and $1.72 \leq D_f \leq 1.90$ (Fig. 6). The predicted boundary curves l_{CF} and l_{CD}, as depicted in Fig. 6, align well with the simulation results.

3.3 Evaluation using experiments in the literature

The predicted phase diagram is further validated using experimental results from the literature (Jung et al., 2016; Hu et al., 2019). In the experiment by Hu et al. (2019), the contact angle is $\theta = 67°$, porosity is $\phi = 0.56$, and the disorder is varied as $\lambda/\lambda_{max} = 0,\ 0.23,\ 0.47$, and 0.70. For $\lambda/\lambda_{max} = 0$ and 0.23 the displacement pattern is CD (red circles in Fig. 7(a)), while for $\lambda/\lambda_{max} = 0.47$ and 0.70 the displacement pattern is the CZ (green circles in Fig. 7(a)). In the experiment by Jung et al. (2016), two microfluidic geometries were employed. One geometry has $\phi = 0.85$, and $\lambda/\lambda_{max} = 0.69$, while the other has $\phi = 0.7$, and $\lambda/\lambda_{max} = 0.41$. Two fluid pairs were used with contact angles of $\theta = 46°$ and 79°. For $\theta = 46°$, CD is observed in both geometries (Fig. 7(b)), whereas for $\theta = 79°$, a CZ is observed in both geometries (Fig. 7(c)). As shown in Fig. 7, the experimental points representing various displacement patterns fall within or very close to the corresponding regions of the predicted phase diagram. Consequently, our theoretical

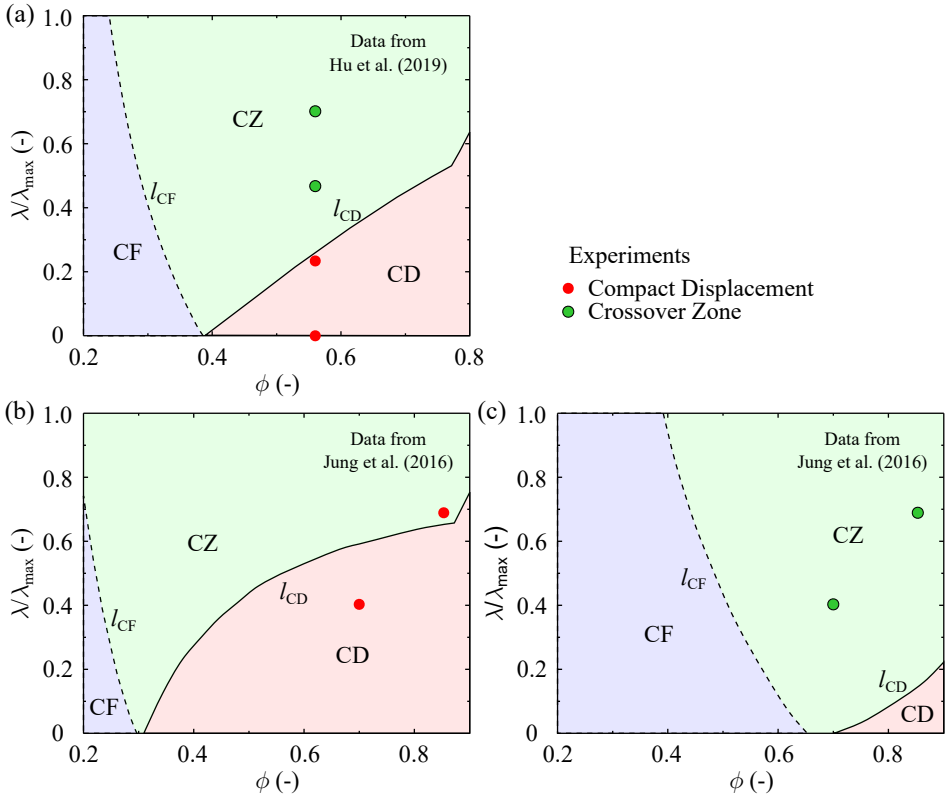

Fig. 7. Evaluation of the phase diagram using experiment data from the literature (Jung et al., 2016; Hu et al., 2019). The phase diagram is recalibrated to align with experimental conditions, featuring (a) $\theta = 67°$, (b) $\theta = 46°$, and (c) $\theta = 79°$. The experimental data are represented by red circles for the CD and green circles for the CZ. The dashed line and solid lines, derived from the theoretical model, depict the transition of displacement patterns from CF to CZ and from CZ to CD, respectively.

model can reasonably predict the transition of displacement patterns under varying porosity and disorder.

4. Conclusions

A combination of pore-network simulations and a theoretical model is employed to investigate the transition of displacement patterns under varying porosity and disorder. Through theoretical analysis of the probability of overlap events, which stabilize the invasion front, a model is proposed to describe the transition of displacement patterns from CF to the CZ and then to CD. The predicted phase diagram is evaluated using pore-network simulations and experimental data from the literature.

Unlike previous studies that consider factors such as flow rate, wetting conditions, and fluid properties, our model can predict displacement patterns under arbitrary flow geometries with given porosity and disorder. Consequently, our work extends the classic phase diagram to incorporate the influence of porosity and disorder in porous media. This research holds practical significance for engineering applications, including geological carbon sequestration, oil recovery, and shale gas production.

Acknowledgements

This work was supported by the National Natural Science Foundation of China (No. 52309141) and the Fundamental Research Funds for the Central Universities (No. 2042023kfyq03).

Conflict of interest

The authors declare no competing interest.

References

Al-Housseiny, T. T., Tsai, P. A., Stone, H. A. Control of interfacial instabilities using flow geometry. Nature Physics, 2012, 8(10): 747-750.

Armstrong, R. T., Berg, S. Interfacial velocities and capillary pressure gradients during Haines jumps. Physical Review E, 2013, 88(4): 043010.

Babchin, A., Brailovsky, I., Gordon, P., et al. Fingering instability in immiscible displacement. Physical Review E, 2008, 77(2): 026301.

Bischofberger, I., Ramachandran, R., Nagel, S. R. Fingering versus stability in the limit of zero interfacial tension. Nature Communications, 2014, 5(1): 5265.

Borgman, O., Fantinel, P., Lühder, W., et al. Impact of spatially correlated pore scale heterogeneity on drying porous media. Water Resources Research, 2017, 53(7): 5645-5658.

Cai, J., Jin, T., Kou, J., et al. Lucas-Washburn equation-based modeling of capillary-driven flow in porous systems. Langmuir, 2021, 37(5): 1623-1636.

Cai, J., Perfect, E., Cheng, C. L., et al. Generalized modeling of spontaneous imbibition based on Hagen-Poiseuille flow in tortuous capillaries with variably shaped apertures. Langmuir, 2014, 30(18): 5142-5151.

Cai, J., Yu, B., Zou, M., et al. Fractal characterization of spontaneous co-current imbibition in porous media. Energy & Fuels, 2010, 24(3): 1860-1867.

Chen, J., Wilkinson, D. Pore-scale viscous fingering in porous media. Physical Review Letters, 1985, 55(18): 1892-1895.

Chen, Y., Fang, S., Wu, D., et al. Visualizing and quantifying the crossover from capillary fingering to viscous fingering in a rough fracture. Water Resources Research, 2017, 53(9): 7756-7772.

Cieplak, M., Robbins, M. O. Dynamical transition in quasi-static fluid invasion in porous-media. Physical Review Letters, 1988, 60(20): 2042-2045.

Cieplak, M., Robbins, M. O. Influence of contact-angle on quasi-static fluid invasion of porous-media. Physical Review B, 1990, 41(16): 11508.

Concus, P., Finn, R. On the behavior of a capillary surface in a wedge. Proceeding of the National Academy of Sciences of the United States of America, 1969, 63(2): 292-299.

Cottin, C., Bodiguel, H., Colin, A. Influence of wetting conditions on drainage in porous media: A microfluidic study. Physical Review E, 2011, 84(2): 026311.

Dawson, H. E., Roberts, P. V. Influence of viscous, gravitational, and capillary forces on dnapl saturation. Ground Water, 1997, 35 (2): 261-269.

de Anna, P., Quaife, B., Biros, G., et al, Prediction of the low-velocity distribution from the pore structure in simple porous media. Physical Review Fluids, 2017, 2(12): 124103.

Dong, M., Chatzis, I. The imbibition and flow of a wetting liquid along the corners of a square capillary tube. Journal of Colloid and Interface Science, 1995, 172(2): 278-288.

Ershadnia, R., Wallace, C. D., Soltanian, M. R. CO_2 geological sequestration in heterogeneous binary media: Effects of geological and operational conditions. Advances in Geo-Energy Research, 2020, 4(4): 392-405.

Fantinel, P., Borgman, O., Holtzman, R., et al. Drying in a microfluidic chip: Experiments and simulations. Scientific Reports, 2017, 7(1): 15572.

Geiger-Boschung, S., Matthäi, S. K., Niessner, J., et al. Black-oil simulations for three-component, three-phase flow in fractured porous media. SPE Journal, 2009, 14(2): 338-354.

Geistlinger, H., Zulfiqar, B. The impact of wettability and surface roughness on fluid displacement and capillary trapping in 2-D and 3-D porous media: 1. Wettability-Controlled phase transition of trapping efficiency in Glass beads packs. Water Resources Research, 2020, 56(10): e2019WR026826.

Glass, R., Rajaram, H., Nicholl, M., et al. The interaction of two fluid phases in fractured media. Current Opinion in Colloid & Interface Science, 2001, 6(3): 223-235.

Holtzman, R. Effects of pore-scale disorder on fluid displacement in partially-wettable porous media. Scientific Reports, 2016, 6(1): 36221.

Holtzman, R., Segre, E. Wettability stabilizes fluid invasion into porous media via nonlocal, cooperative pore filling. Physical Review Letters, 2015, 115(16): 164501.

Hu, R., Lan, T., Wei, G., et al. Phase diagram of quasi-static immiscible displacement in disordered porous media. Journal of Fluid Mechanics, 2019, 875: 448-475.

Hu, R., Wan, J., Yang, Z., et al. Wettability and flow rate impacts on immiscible displacement: A theoretical model. Geophysical Research Letters, 2018, 45(7): 3077-3086.

Jung, M., Brinkmann, M., Seemann, R., et al. Wettability controls slow immiscible displacement through local interfacial instabilities. Physical Review Fluids, 2016, 1(7): 074202.

King, P. R. The fractal nature of viscous fingering in porous media. Journal of Physics A-Mathematical and General, 1987, 20(8): L529.

Lan, T., Hu, R., Guo, W., et al. Direct prediction of fluid-fluid displacement efficiency in ordered porous media using the pore structure. Water Resources Research, 2022a, 58(7): e2021WR031875.

Lan, T., Hu, R., Yang, Z., et al. Transitions of fluid invasion patterns in porous media. Geophysical Research Letters, 2020, 47(20): e2020GL089682.

Lan, T., Hu, R., Yang, Z., et al. A pore filling-based model to predict quasi-static displacement patterns in porous media with pore size gradient. Frontiers in Physics, 2022b, 10: 993398.

Lenormand, R., Touboul, E., Zarcone, C. Numerical models and experiments on immiscible displacements in porous media. Journal of Fluid Mechanics, 1988, 189: 165-187.

Levaché, B., Bartolo, D. Revisiting the Saffman-Taylor experiment: Imbibition patterns and liquid-entrainment transitions. Physical Review Letters, 2014, 113(4): 044501.

Lewandowska, J., Szymkiewicz, A., Auriault, J. L. Upscaling of Richards' equation for soils containing highly conductive inclusions. Advances in Water Resources, 2005, 28(11): 1159-1170.

Li, G., Zhan, L., Yun, T., et al. Pore-scale controls on the gas and water transport in hydrate-bearing sediments. Geophysical Research Letters, 2020, 47(12): e2020GL086990.

Lu, N. B., Browne, C. A., Amchin, D. B., et al. Controlling capillary fingering using pore size gradients in disordered media. Physical Review Fluids, 2019, 4(8): 084303.

Måløy, K., Feder, J., Jossang, T. Viscous fingering fractals in porous-media. Physical Review Letters, 1985, 55(24): 2688-2691.

Molnar, I. L., Gerhard, J. I., Willson, C. S., et al. Wettability effects on primary drainage mechanisms and NAPL distribution: A pore-scale study. Water Resources Research, 2020, 56(1): e2019WR025381.

Morrow, N. R., Mason, G. Recovery of oil by spontaneous imbibition. Current Opinion in Colloid & Interface Science, 2001, 6(4): 321-337.

Nijjer, D., Hewitt, D., Neufeld, J. A. Stable and unstable miscible displacements in layered porous media. Journal of Fluid Mechanics, 2019, 869: 468-499.

Odier, C., Levache, B., Santanach-Carreras, E., et al. Forced imbibition in porous media: A fourfold scenario. Physical Review Letters, 2017, 119(20): 208005.

Paterson, L. Radial fingering in a Hele Shaw cell. Journal of Fluid Mechanics, 1981, 113: 513-529.

Pi, Z., Peng, H., Jia, Z., et al. Coupling mechanisms of displacement and imbibition in pore-fracture system of tight oil reservoir. Capillarity, 2023, 7(1): 13-24.

Primkulov, B. K., Pahlavan, A. A., Fu, X., et al. Signatures of fluid-fluid displacement in porous media: Wettability, patterns and pressures. Journal of Fluid Mechanics, 2019, 875: R4.

Primkulov, B. K., Pahlavan, A. A., Fu, X., et al. Wettability and Lenormand's diagram. Journal of Fluid Mechanics, 2021, 923: A34.

Primkulov, B. K., Talman, S., Khaleghi, K., et al. Quasistatic fluid-fluid displacement in porous media: Invasion-percolation through a wetting transition. Physical Review Fluids, 2018, 3(10): 104001.

Rabbani, H. S., Or, D., Liu, Y., et al. Suppressing viscous fingering in structured porous media. Proceeding of the National Academy of Sciences of the United States of America, 2018, 115(19): 4833-4838.

Roof, J. G. Snap-off of oil droplets in water-wet pores. Society of Petroleum Engineers Journal, 1970, 10(1): 85-90.

Singh, K., Jung, M., Brinkmann, M., et al. Capillary-dominated fluid displacement in porous media. Annual Review of Fluid Mechanics, 2019, 51(1): 429-449.

Spaid, M. A. A., Phelan, F. R. Modeling void formation dynamics in fibrous porous media with the lattice Boltzmann method. Composites Part A-Applied Science and Manufacturing, 1998, 29(7): 749-755.

Suo, S., Liu, M., Gan, Y. Fingering patterns in hierarchical porous media. Physical Review Fluids, 2020, 5(3): 034301.

Svidrytski, A., Rathi, A., Hlushkou, D., et al. Morphology of fluids confined in physically reconstructed mesoporous silica: Experiment and mean field density functional theory. Langmuir, 2018, 34(34): 9936-9945.

Tang, H., Wang, S., Pan, M., et al. Porosity-graded microporous layers for polymer electrolyte membrane fuel cells. Journal of Power Sources, 2007, 166(1): 41-46.

Toussaint, R., Lovoll, G., Méheust, Y., et al. Influence of pore-scale disorder on viscous fingering during drainage. Europhysics Letters, 2005, 71(4): 583-589.

Wang, Y., Shang, Q., Guo, J., et al. Study on imbibition during the CO_2 enhanced oil recovery in fractured tight sandstone reservoirs. Capillarity, 2023, 7(3): 47-56.

Wang, Z., Pereira, J. M., Sauret, E., et al. Emergence of unstable invasion during imbibition in regular porous media. Journal of Fluid Mechanics, 2022, 941: A40.

Wei, B., Wang, B., Li, X., et al. CO_2 storage in depleted oil and gas reservoirs: A review. Advances in Geo-Energy Research, 2023, 9(2): 76-93.

Weislogel, M. M., Lichter, S. Capillary flow in an interior corner. Journal of Fluid Mechanics, 1998, 373: 349-378.

Wu, D., Hu, R., Lan, T., et al. Role of pore-scale disorder in fluid displacement: Experiments and theoretical model. Water Resources Research, 2021, 57(1): e2020WR028004.

Zhao, B., MacMinn, C. W., Juanes, R. Wettability control on multiphase flow in patterned microfluidics. Proceeding of the National Academy of Sciences of the United States of America, 2016, 113(37): 10251-10256.

Zhao, B., MacMinn, C. W., Primkulov, B. K., et al. Comprehensive comparison of pore-scale models for multiphase flow in porous media. Proceeding of the National Academy of Sciences of the United States of America, 2019, 116(28): 13799-13806.

Zhao, J., Yang, L., Qin, F., et al. Pore-scale fluid flow simulation coupling lattice Boltzmann method and pore network model. Capillarity, 2023, 7(3): 41-46.